An Integrated Power Decoupling Method for Single-Phase EV Onboard Charger in V2G Application

Yuxuan Bi, Chao Wu, *Member, IEEE*, Junzhong Xu, *Member, IEEE*, Houji Li, *Student Member, IEEE*, Yong Wang, *Member, IEEE*, Guohua Shu, and Thiago Batista Soeiro, *Senior Member, IEEE*

***Abstract*—Instead of bulky passive filters, the active power decoupling (APD) method can be adopted to suppress the second-order ripple power in the dc bus of the single-phase electric vehicle onboard charging system. However, the traditional APD methods require additional power switches and energy storage devices, which increase the cost and significantly reduce the power conversion efficiency. To tackle these problems, an integrated method of utilizing the auxiliary power module to form a series-connected APD circuit is proposed in this article. Without additional switches and energy storage devices, the APD circuit only needs to compensate less than 10% of the rated power, while realizing soft-switching operation. In addition, the corresponding control method can further reduce the voltage stress of the switches on the high-voltage side of the converter, and increase the efficiency of the system. Finally, a 2-kW single-phase charging system prototype is built to verify the feasibility and effectiveness of the proposed method.**

***Index Terms*—Active power decoupling (APD), auxiliary power modules, second-order current ripple suppression, single-phase onboard charging system, soft-switching.**

I. Introduction

TO ACCELERATE the promotion of carbon neutrality, electric vehicles (EVs) have been developed due to their characteristics of high efficiency and low pollution emission [1], [2], [3]. The widespread use of the EVs makes them not only regarded as loads, but also as power resources, that is, to realize vehicle-to-grid (V2G) operation, of which the economic benefits have been widely concerned in the past decades [4], [5], [6]. The structure diagram of a typical EV, including its single-phase onboard battery charging system, is shown in Fig. 1. However, in this system, the ripple power at twice the grid frequency on the grid side will cause a low-frequency voltage or current ripples on the dc bus, which is harmful to the reliability and the control performance, such as the efficiency and power quality. In fact, the second-order ripple voltage on the dc bus could not only lead to the distortion of the input current [7], but also affects all the loads connected to the dc bus [8]. In addition, the low-frequency ripple currents may affect the lifetime of the battery and the reliability of the system [9].

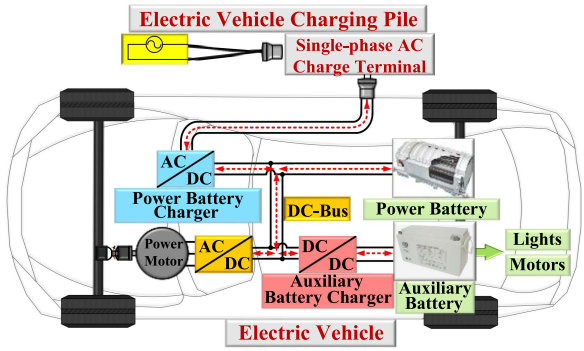

Fig. 1. Structure diagram of a typical EV, including the single-phase EV onboard charging system.

To solve these inherent problems, the most common method is to add a bulky passive filtering device at the dc bus [10], [11]. However, the volume and weight of the converter will be significantly increased, and the short lifetime of the electrolytic capacitor will affect the reliability of the system [12]. In order to reduce the requirements for the passive components on the dc bus, the active power decoupling (APD) method has become a research hotspot in recent years. According to the type of energy storage devices used, the APD methods can be divided into inductive- or capacitive-types methods [13], [14]. The capacitive-type APD methods are the most commonly used because they lead to higher power density designs. Examples of capacitive type APD circuits are shown in Fig. 2. The buck, boost, buck–boost, and full-bridge types APD methods are shown in Fig. 2(a)–(d), respectively [15], [16], [17], [18]. It is noted that the above methods all require additional switches to form the APD circuit, as shown in Fig. 2(e) and (f), the number of the power switches can be reduced by multiplexing switches to achieve power factor correction (PFC) and APD

Manuscript received 20 December 2022; revised 6 April 2023; accepted 16 May 2023. Date of publication 29 May 2023; date of current version 21 June 2023. Recommended for publication by Associate Editor M. J. Scott. *(Corresponding author: Junzhong Xu.)*

Yuxuan Bi, Chao Wu, Junzhong Xu, Houji Li, Yong Wang, and Guohua Shu are with the Key Laboratory of Control of Power Transmission and Conversion of Ministry of Education, Department of Electrical Engineering, Shanghai Jiao Tong University, Shanghai 200240, China (e-mail: biyuxuan@sjtu.edu.cn; wuchao@sjtu.edu.cn; junzhongxu@sjtu.edu.cn; lihoushen@sjtu.edu.cn; wangyong75@sjtu.edu.cn; shuguohua@sjtu.edu.cn).

Thiago Batista Soeiro is with the Faculty of Electrical Engineering, Mathematics and Computer Science, University of Twente, 7522 NB Enschede, Netherlands (e-mail: t.batistasoeiro@utwente.nl).

Color versions of one or more figures in this article are available at https://doi.org/10.1109/TPEL.2023.3281085.

Digital Object Identifier 10.1109/TPEL.2023.3281085

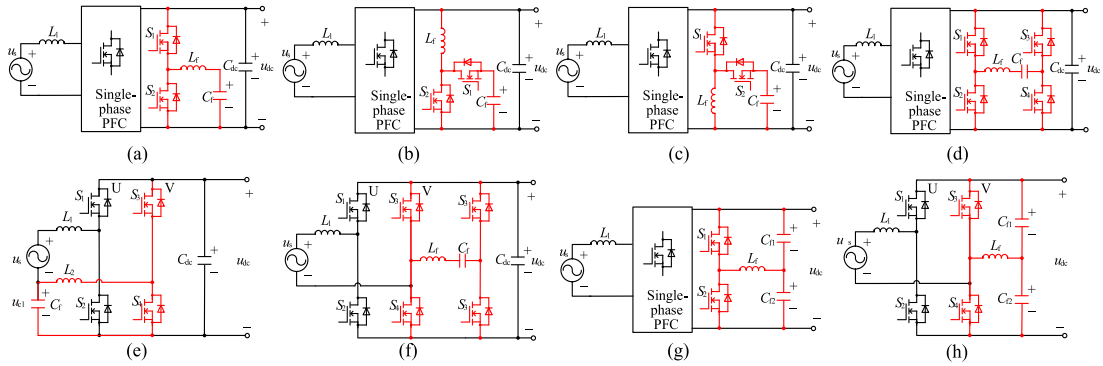

Fig. 2. Single-phase AC–DC converters with APD function: (a) buck type, (b) boost type, (c) buck–boost type, (d) full-bridge type, (e) integrated buck type, (f) flying capacitors type, (g) and (h) DC-split-capacitor type.

functions [19], [20], [21]. However, in these methods, the control loops of the PFC and APD functions are coupled together, which will increase the complexity of the control scheme. In addition, the dc bus capacitors in the above methods are not involved in the APD function, which increase the required filter capacitance. As shown in Fig. 2(g) and (h), the dc split-capacitor type APD methods are proposed in [22], [23], [24], and [25], where both the dc bus capacitors are used to suppress ripple power. However, the control performance of these methods is affected by the asymmetry of the capacitances. Therefore, robust schemes for the capacitance mismatch are proposed in [26] and [27]. Nevertheless, these methods will make the control scheme more complex and increase the computational burden of the controller. At the same time, the above methods need to add passive components or switches compared to the traditional topology, which have a negative impact on the cost of the system.

In order to further improve the power density and reduce the cost of the converter, many researchers are committed to the APD circuit composed of the existing modules in the charging system. In [28], an APD scheme in the control loop of the dc–dc converter in a two-stage inverter is proposed. However, according to the expression of the input instantaneous power on the grid side, the instantaneous power of the dc–dc converter is up to twice the rated power, which has a great impact on the cost and efficiency of the charging system. In the EV charging system, the auxiliary battery is used for the power supply of the lighting system, low-voltage motors, and other components, and thus the auxiliary power module is an essential structure. In [29] and [30], the APD circuits shown in Fig. 2(a) and (g) are formed by changing the structure of the auxiliary power module. In addition, a central-tap is introduced to the high-frequency transformer of the auxiliary power charger, and a filter capacitor is added to realize the APD function [31]. However, these methods still need additional energy storage devices, and the asymmetry of the transformer windings may lead to additional power losses. In [32], an integrated high- and low-frequency ripple suppression method in the EV charging system is proposed. Through the structural design of the auxiliary power module, the APD function can be realized without additional energy storage devices. However, the peak value of the input active power and the second-order ripple power on the grid side is almost the same, while the above methods require the auxiliary power module to handle all the ripple power, resulting in an increase in the cost and a decline in the converter efficiency. In [33], a single-stage converter that can be applied to a single-phase photovoltaic (PV) inverter is proposed, which improves the PV operating range and realizes the APD function by adding additional converters. With this structure, the compensation power of the APD circuit can be significantly reduced. However, this method requires additional switches and capacitors, and increases the voltage stress of the switches and reduces the efficiency of the converter. In addition, it cannot operate in bidirectional power flow.

To solve the aforementioned problems, this article proposes an integrated APD method for the single-phase charging system, which is suitable for V2G applications. In the proposed method, the APD circuit is formed of the auxiliary power module when the EV is parked. The bus capacitors are connected in series and are both used to absorb the pulsating power from the grid side, thereby reducing the required dc bus capacitance, improving the power quality on the grid side, and suppressing the low-frequency ripple current of the power battery. Compared with the existing APD methods, no additional power switches and energy storage devices are needed in the proposed method. In addition, the compensation power of the APD circuit is less than 10% of the ripple power, and the soft-switching operation of the APD circuit can be achieved. Moreover, the corresponding control method can further reduce the voltage stress of the high-voltage side switches, and increases the efficiency of the system. Finally, the feasibility and effectiveness of the proposed method are verified by experimental results.

The rest of this article is organized as follows. In Section II, the onboard charging system is described. The proposed APD method is elaborated in Section III. In Section IV, the experimental results of the 2-kW prototype are presented and discussed. Finally, Section V concludes this article.

II. System Description and Problem Statement

A. Structure of the Adopted EV Charging System

In the onboard charging system of EVs, by reasonably designing the auxiliary power module, the low-frequency current ripple of the power battery can be suppressed in the charging and V2G

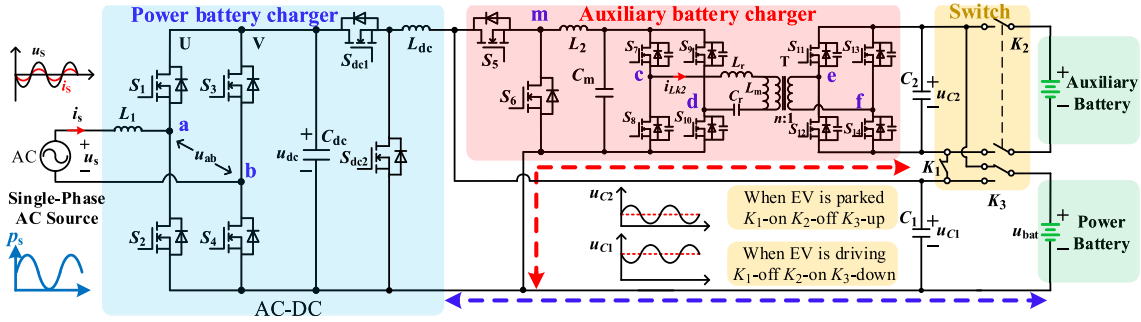

Fig. 3. Structure diagram of the power battery and auxiliary battery charging system.

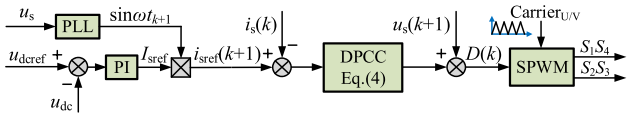

Fig. 4. Control block diagram of the single-phase AC–DC converter in the charging system.

modes when the EV is parked. The adopted structure of power and auxiliary power module is shown in Fig. 3. The high-voltage power battery charger consists of a single-phase H-bridge and a dc–dc converter, including six power switches S_1–S_4, $S_{\rm dc1}$, and $S_{\rm dc2}$, grid side filter inductor L_1, dc filter inductor $L_{\rm dc}$, and dc bus capacitor $C_{\rm dc}$ and C_1.

The auxiliary battery charger comprises an isolated dc–dc converter composed of a buck/boost circuit cascaded with an LLC converter. The main components of this circuit are the switches S_5–S_{14}, the high-frequency transformer T, the resonant tank with inductors L_r and L_m and capacitor C_r, and the bus capacitor C_m and C_2.

The auxiliary battery charger has two different operation modes during the driving charging and parking charging of the EV. When the EV is running, the switch K_1 on the battery side is OFF, K_2 is ON, and the lower contact of K_3 is ON, which means the power battery and auxiliary battery are completely decoupled under this situation. The auxiliary power charger can control the power flow of the charging and discharging operation of the auxiliary battery. When the EV is parked, K_1 is ON, K_2 is OFF, and the upper contact of K_3 is ON, thus forming an APD circuit with series-connected bus capacitors, which enables these capacitors to absorb the ripple power simultaneously. On the one hand, it can suppress the low-frequency voltage or current ripple generated during the operation of the single-phase ac–dc converter, it reduces the required bus capacitance, and can prolong the service life of the power battery. On the other hand, due to the series-connection of the bus capacitors, u_{C1} is less than the power battery voltage $u_{\rm bat}$, which can reduce the voltage stress of the switches in the ac–dc converter of the power battery charger and the buck/boost converter of the auxiliary battery charger compared to traditional methods, and thus reducing the switching loss.

In the adopted charging system, the control loop of the single-phase ac–dc converter is shown in Fig. 4, which can be divided into dc bus voltage loop and input current loop. A PI controller is used in the voltage loop to make the dc bus voltage $u_{\rm dc}$ stable and to track the reference $u_{\rm dcref}$. A deadbeat predictive current control (DPCC) method is adopted in the current loop to achieve the PFC function of the grid side current i_s with fast dynamic performance. In addition, the second-order generalized integral phase-locked loop is adopted. To compensate for the influence of control delay, the DPCC scheme generally predicts the system state in the $(k+1)$th sample to improve the control performance, and the phase of the reference current $i_{\rm sref}$ of the $(k+1)$th sample can be obtained as

$$\omega t_{k+1} = \omega t_k + \frac{2\pi T_s}{T_{\rm grid}} \tag{1}$$

where T_s and $T_{\rm grid}$ are the control cycle and the grid cycle, respectively. In Fig. 3, the equation of the single-phase ac–dc converter satisfying Kirchhoff's voltage law can be written as

$$u_s = L_1 \frac{{\rm d}i_s}{{\rm d}t} + u_{ab} = L_1 \frac{{\rm d}i_s}{{\rm d}t} + D_{ab} u_{\rm dc} \tag{2}$$

where D_{ab} refers to the calculated modulation of the single-phase ac–dc converter, and it meets $-1 < D_{ab} < 1$. The input currents at the $(k+1)$th and $(k+2)$th samples are predicted to reduce the impact of the control delay on the current control performance of the DPCC [6], [7], and it can be approximately considered that ${\rm d}i_s/{\rm d}t = [i_s(k+1) - i_s(k)]/T_s = [i_s(k+2) - i_s(k+1)]/T_s$, so it can be deduced that

$$\begin{cases} i_s(k+1) = i_s(k) + \frac{T_s}{L_1}\left[u_s(k) - u_{ab}(k)\right] \\ i_s(k+2) = i_s(k+1) + \frac{T_s}{L_1}\left[u_s(k+1) - u_{ab}(k+1)\right]. \end{cases} \tag{3}$$

The DPCC method aims to make the predicted input current equal to [7], that is, $i_s(k+2) = i_{\rm sref}(k+1)$, and thus the expression of D_{ab} can be derived as

$$D_{ab} = \frac{u_s(k+1) - \frac{L_1}{2T_s}\left[i_{\rm sref}(k+1) - i_s(k)\right]}{u_{\rm dc}}. \tag{4}$$

Due to the lower efficiency and higher cost of the system when adopting the APD schemes in the dc–Dc converter of the power battery charger [28], [32], no ripple suppression schemes are used in the power battery charger. In addition, to simplify the analysis of the APD method, $S_{\rm dc1}$ is turned ON, $S_{\rm dc2}$ is turned OFF, and $C_{\rm bus}$ is set as the equivalent bus capacitance of the power battery charger, which is equal to $C_1 + C_{\rm dc}$.

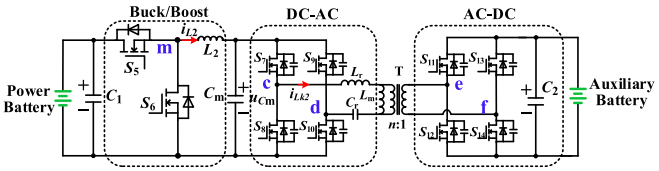

Fig. 5. Charging structure of the auxiliary battery in driving charging mode.

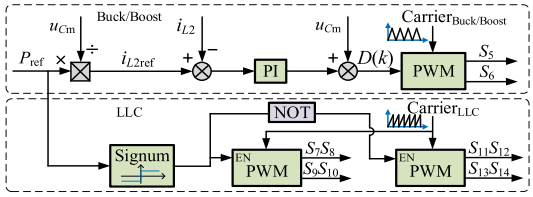

Fig. 6. Control block diagram of the buck/boost and the LLC converter in driving charging mode.

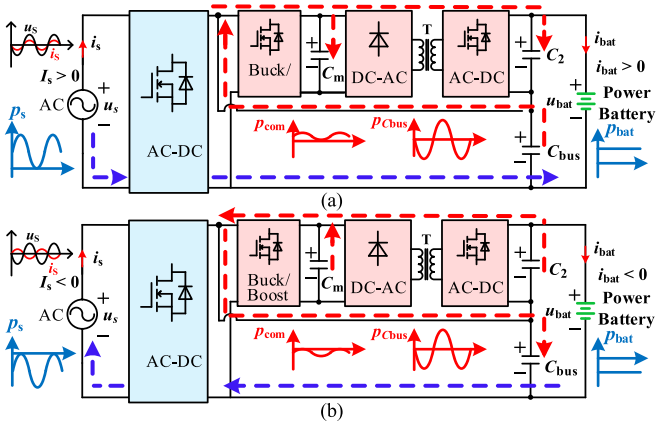

Fig. 7. Structure of the EV charging system when the EV is parked with the proposed APD method: (a) charging mode and (b) V2G mode.

In the driving charging mode, the structure of the auxiliary battery charger is shown in Fig. 5, which is adopted for the power supply of lighting systems, motors, and other electrical appliances. Considering the requirements of bidirectional operation and the soft-switching range, a two-stage dc–dc converter is adopted. Its control method is shown in Fig. 6. The buck/boost converter is adopted to control the power flow between the power battery and the auxiliary battery through the inductor current loop, and the LLC converter is used as a dc transformer and operates at a fixed switching frequency at slightly under the resonant operating point. By judging the value of the reference power $P_{\rm ref}$, the LLC converter makes the dc–ac part or ac–dc part operate, respectively, when $P_{\rm ref} > 0$ and $P_{\rm ref} < 0$, while the other part conducts uncontrolled rectification through parallel diodes. In addition, it is worth noting that the buck/boost converter uses a triangular carrier to sample the average value of i_{L2} for closed-loop inductor current control, while the LLC circuit uses a sawtooth carrier to improve the carrier accuracy in the digital controller.

B. DC-Side Second-Order Ripple Power Analysis

When the system is operating in parking charging mode, assuming that u_s and i_s are ideal sinewaves, and the angular frequency of the grid is ω, it follows that

$$\begin{cases} u_s = \sqrt{2}U_s \sin\omega t \\ i_s = \sqrt{2}I_s \sin(\omega t + \theta) \end{cases} \tag{5}$$

where U_s and I_s correspond to the rms value of the grid voltage and current, respectively, θ is the phase difference between u_s and i_s, that is, the power factor angle. When considering the reactive power absorbed by the filter inductor L_1, the expression of the instantaneous power $p_{\rm in}$ of the dc side can be derived as

$$\begin{aligned} p_{\rm in} &= p_s + p_{L1} = u_s i_s + L_1 \frac{{\rm d}i_s}{{\rm d}t} i_s \\ &= \underbrace{U_s I_s \cos\theta}_{P_{\rm in}} \underbrace{- U_s I_s \cos(2\omega t + \theta) - \omega L_1 I_s^2 \sin(2\omega t + 2\theta)}_{p_{2\omega}}. \end{aligned} \tag{6}$$

It can be seen from (6) that $p_{\rm in}$ consists of the dc component $P_{\rm in}$ and the second-order ripple component $p_{2\omega}$. If all the second-order ripple power is absorbed by the power battery, that is, $p_{\rm bat} = p_{\rm in}$, the input current of the power battery $i_{\rm bat}$ can be expressed as

$$i_{\rm bat} = \frac{p_{\rm in}}{u_{\rm bat}} = \frac{P_{\rm in}}{u_{\rm bat}} - \frac{P_{2\omega}}{u_{\rm bat}} \sin(2\omega t + \varphi) \tag{7}$$

where $P_{2\omega} = I_s(U_s{}^2 + \omega^2 L_1{}^2 I_s{}^2)^{1/2}$ and $\varphi = \arctan(U_s/\omega L_1 I_s)$. It is noted that the input current of the power battery contains a large second-order current ripple, which will cause the battery to overheat and affect its lifetime of the battery. Moreover, the second-order component of the dc bus voltage will lead to the degradation of the grid side power quality. The application of the APD circuit can suppress the second-order ripple power through the energy storage capacitor, extend the lifetime of the power battery, reduce the required bus capacitance, and improve the power density and the control performance of the converter. In addition, it is necessary to propose an effective corresponding power decoupling control method.

III. Analysis of the Proposed APD Method

A. Power Decoupling Control Method

When the EV is parked, bus capacitors C_1 and C_2 can be connected in series by controlling the switches K_1, K_2, and K_3, and the proposed APD circuit composed of the auxiliary power charger can be obtained to suppress the second-order ripple current of the power battery, without additional power switches and bulky passive filters. The onboard charging system can be operated in the charging mode and the V2G mode, as shown in Fig. 7.

According to the power conservation, the sum of the power of the battery and the power of the bus capacitors is equal to the $p_{\rm in}$ obtained by (6). In order to stabilize the bus voltage and reduce the ripple current of the battery, the power battery and bus capacitors are supposed to absorb the dc part and the ripple part of $p_{\rm in}$, respectively. Therefore, the power expression of the

dc side can be obtained as follows:

$$\begin{cases} p_{\text{bat}} = P_{\text{in}} \\ \sum p_{Ci} = \sum C_i u_{Ci} \frac{\mathrm{d}u_{Ci}}{\mathrm{d}t} = p_{2\omega}. \end{cases} \tag{8}$$

The aim of the power decoupling control method is to make the voltage of the capacitors C_1 and C_2 change with twice the grid frequency, and thus absorb the ripple power of the dc side. In the structure shown in Fig. 7, when the system is in charging or V2G operation, the bus capacitors C_{bus} and C_2 are both used for active filtering, and $u_{C1} + u_{C2} = u_{\text{bat}}$. Thus, it can be obtained that

$$\begin{cases} u_{C1} = (1-m)\, u_{\text{bat}} - u_{\text{apd}} \\ u_{C2} = m u_{\text{bat}} + u_{\text{apd}} \end{cases} \tag{9}$$

where m is the dc voltage coefficient of C_2, which determines the voltage division ratio of C_1 and C_2 in u_{bat}, and the steady-state operating point of the APD method, and thus it is necessary to calculate the optimal value of m in the adopted control method.

Affected by the dc voltage gain limitation of the auxiliary power charger, the range of m is $0 < m < 1/n$, in which n is the ratio of the high-frequency transformer T. u_{apd} is the fluctuation component of u_{C1} and u_{C2}. According to (8) and (9), it can be deduced that

$$u_{\text{apd}} = -A_1 u_{\text{bat}} \pm \sqrt{A_1^2 u_{\text{bat}}^2 + \frac{P_{2\omega}}{\omega\,(C_{\text{bus}} + C_2)} \cos(2\omega t + \varphi)} \tag{10}$$

where $A_1 = [C_{\text{bus}} + m(C_2 - C_{\text{bus}})]/(C_{\text{bus}} + C_2)$. It can be seen from (10) that the u_{C1} and u_{C2} are required to fluctuate at twice the grid frequency to realize second-order ripple power decoupling. At the same time, the amplitude of the fluctuation component u_{apd} can be approximately obtained as

$$U_{\text{apd}} = -A_1 u_{\text{bat}} + \sqrt{A_1^2 u_{\text{bat}}^2 + \frac{P_{2\omega}}{\omega\,(C_{\text{bus}} + C_2)}}. \tag{11}$$

It can be seen from (11) that the amplitude of the voltage fluctuation component of u_{C1} and u_{C2} is related to the input power, the capacitance of C_{bus} and C_2, and the voltage coefficient m. At the same time, due to the limitation of the converter topology, $u_{C2} > 0$, so the setting value of m meets that

$$m u_{\text{bat}} > U_{\text{apd}}. \tag{12}$$

According to (11) and (12), the relationship between $U_{\text{apd}}/u_{\text{bat}}$, bus capacitances, and m can be obtained when $P_{\text{in}} \approx P_{2\omega} = 2$ kW, as shown in Fig. 8(a). It can be seen that $U_{\text{apd}}/u_{\text{bat}}$ decreases with the increase of the proportion of C_{bus} in the sum of dc bus capacitance ΣC_i, and also decreases with the increase of ΣC_i. In addition, when $C_{\text{bus}}/\Sigma C_i$ is relatively large, U_{apd} will be smaller as m decreases. When $C_{\text{bus}}/\Sigma C_i$ is close to 0, U_{apd} will increase as m decreases. In addition, Fig. 8(a) shows a plane of $U_{\text{apd}} = m u_{\text{bat}}$, and only the points below this plane meet the operating requirements of the APD circuit. It can be seen that the higher $C_{\text{bus}}/\Sigma C_i$ is, the larger the scope of meeting the operation requirements of the proposed method is. At the same time, with the increase of m, the average value of u_{C1} is lower, which can further reduce the voltage stress of the switches of the previous power battery charger and the APD circuit, thus improving the

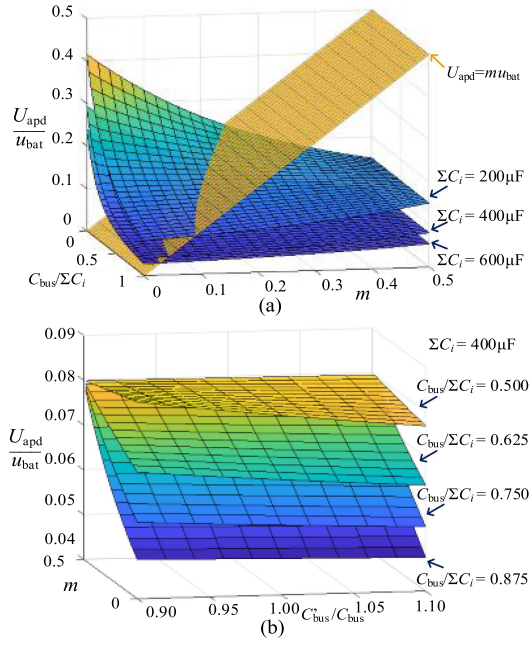

Fig. 8. Relationship between $U_{\text{apd}}/u_{\text{bat}}$, bus capacitances, and m (a) considering the impact of $C_{\text{bus}}/\Sigma C_i$ and (b) considering the impact of capacitance mismatch of C_{bus}.

efficiency of the converter. It is noted that the accuracy of the bus capacitance will affect the reference voltage calculated, thereby affecting the APD control performance. The impact of the C'_{bus} in the converter and the capacitance parameter C_{bus} in the controller is shown in Fig. 8(b). By adopting APD methods, film capacitors, rather than electrolytic capacitors, with smaller capacitance but higher accuracy can be used as bus capacitors. In addition, it can be seen that as $C_{\text{bus}}/\Sigma C_i$ increases, the impact of capacitance mismatch on the reference voltage is smaller.

On the other hand, as the output voltage range of the auxiliary power module in the EV is generally much lower than that of the power battery, the withstand voltage value of the switches and C_2 in the ac–dc part of the LLC is generally low. In addition, due to the topology of the buck/boost converter, $n u_{C2} = u_{Cm} < u_{C1}$. Therefore, from (9), it can be obtained that

$$\begin{cases} m u_{\text{bat}} \le U_{\text{LVmax}} - U_{\text{apd}} \\ m n u_{\text{bat}} + n U_{\text{apd}} \le (1-m)\, u_{\text{bat}} - U_{\text{apd}} \end{cases} \tag{13}$$

where U_{LVmax} is the maximum withstand voltage of the low-voltage side of the LLC. To ensure sufficient margin, the selected U_{LVmax} is less than u_{C1}/n. At the same time, in order to improve the efficiency of the converter as much as possible, in the control method, it takes that $m u_{\text{bat}} = U_{\text{LV\_max}} - U_{\text{apd}}$. Combined with (11), it can be derived that

$$m = (-C_{\text{bus}} A_2 A_3 + \frac{\sqrt{C_{\text{bus}}^2 A_2^2 A_3^2 - 4 A_2 A_4 \frac{P_{2\omega}}{\omega} - U_{\text{LVmax}}^2 A_2^2 - 2 u_{\text{bat}} U_{\text{LVmax}} C_{\text{bus}} A_2)}}{2 u_{\text{bat}} A_4} \tag{14}$$

where $A_2 = C_{\text{bus}} + C_2$, $A_3 = 2u_{\text{bat}} + 4U_{\text{LV\_max}}$, and $A_4 = -3{C_{\text{bus}}}^2 + {C_2}^2 - 2C_{\text{bus}} C_2$. In addition, it can be seen from Fig. 8

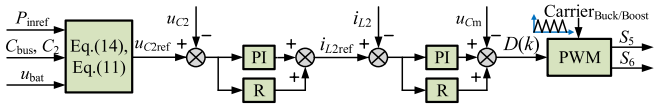

Fig. 9. Control block diagram of the buck/boost in the parking charging mode.

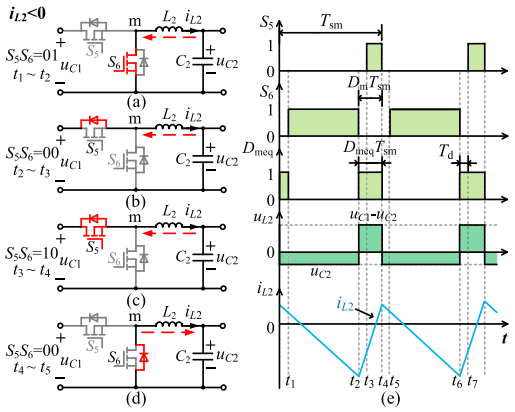

Fig. 10. Operation mode diagram of the buck/boost converter in the V2G operation: (a) $S_5S_6 = 01$, (b) $S_5S_6 = 00$, (c) $S_5S_6 = 10$, (d) $S_5S_6 = 00$, and (e) schematic diagram of i_{L2}.

that when $C_{\rm bus}/\Sigma C_i$ is relatively high, the selection of m has little impact on $U_{\rm apd}$. Therefore, in order to reduce the calculation burden of the controller, $m = 1/(2n)$ can be substituted into (11), and then the required value of m can be calculated as follows:

$$m = \frac{U_{\rm LVmax} - U_{\rm apd}\{m = 1/(2n)\}}{u_{\rm bat}}. \tag{15}$$

To sum up, the control method adopted by the buck/boost converter in the APD circuit is shown in Fig. 9. In the adopted control method, a resonant (R) controller with a central frequency tuned to twice the grid frequency is added to make u_{C2} track the reference $u_{C2\rm ref}$. The control method for the LLC converter is the same as that in Fig. 6, in which the operating direction is selected by the direction of the reference power.

B. Soft-Switching Analysis of the APD Circuit

In order to further improve the efficiency of the proposed APD converter, it is necessary to pay attention to the soft-switching of the APD circuit. Since the LLC converter still operates at a fixed frequency, it can achieve soft-switching operation in a wide load range. The equation of the buck/boost converter is as follows:

$$D_m u_{C1} = L_2 \frac{{\rm d}i_{L2}}{{\rm d}t} + u_{Cm} \tag{16}$$

where D_m is the calculated modulation of the buck/boost, meeting $0 < D_m < 1$. According to (16), the operation states of the buck/boost converter during V2G operation can be obtained, as shown in Fig. 10. In Fig. 10, T_{sm} is the switching frequency of the buck/boost converter and $D_{\rm meq}$ is the equivalent modulation after considering the deadtime T_d. It can be seen that when the waveform of the inductor current i_{L2} has zero-crossing points in every switching cycle, not only can the switches realize ZVS

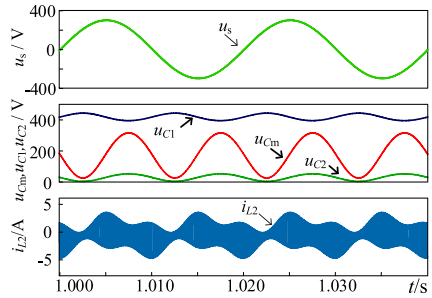

Fig. 11. Main simulation waveforms of the proposed APD circuit in the V2G mode.

[34], [35], but also can ensure that the modulation D_m generated by the controller is equal to the modulation $D_{\rm meq}$ after adding the deadtime in the modulation, that is, the control loop is not affected by the deadtime [36].

The LLC converter can be regarded as a dc transformer with a transformation ratio of n. In addition, while ignoring the second-order ripple power on L_1, that is, $\varphi = \pi/2$, the expression of u_{Cm} can be further obtained as

$$u_{Cm} = nu_{C2} = nmu_{\rm bat} - nU_{\rm apd}\sin 2\omega t. \tag{17}$$

From Figs. 5 and 7, it can be deduced that

$$i_{L2} = C_m \frac{{\rm d}u_{Cm}}{{\rm d}t} + \frac{C_2}{n}\frac{{\rm d}u_{C2}}{{\rm d}t} + \frac{i_{\rm bat}}{n}. \tag{18}$$

When the APD method is adopted and S_5 and S_6 are operating in the critical ZVS, the simulation results of the buck/boost part are shown in Fig. 11. It can be seen from (16) and Fig. 11 that the current ripple of i_{L2} is the smallest when the grid voltage phase ωt is $\pi/4$, which is difficult to achieve ZVS. If the converter can achieve second-order power suppression at this time, it can be obtained that $i_{\rm bat} = P_{\rm in}/u_{\rm bat}$. Thus, it can be derived that the average value I_{L2} of i_{L2} when $\omega t = \pi/4$ is

$$I_{L2} = \frac{P_{\rm in}}{nu_{\rm bat}}. \tag{19}$$

In one switching cycle, the expression of Δi_{L2} when S_5 is equivalently turned ON can be written as

$$\Delta i_{L2} = \frac{D_m T_{sm}(u_{C1} - u_{C2})}{L_2}. \tag{20}$$

To make i_{L2} have zero-crossing points in a switching cycle, it is necessary to meet $I_{L2} < \Delta i_{L2}/2$, that is, to achieve ZVS operation of the buck/boost in the APD circuit in the full load range, the grid-side power is required to meet as follows:

$$\begin{aligned} P_{\rm in} &< \frac{n^2 T_{\rm sm} u_{\rm bat} u_{C2}(u_{C1} - u_{C2})}{2u_{C1}L_2} \\ &= \frac{T_{\rm sm} u_{\rm bat} u_{Cm}(nu_{C1} - u_{Cm})}{2u_{C1}L_2}. \end{aligned} \tag{21}$$

Due to $nu_{C1} >> u_{Cm}$, it is known that as the reference of u_{C2} or u_{Cm} increases, the maximum $P_{\rm in}$ achieving soft-switching also increases. Therefore, in the proposed APD method, while satisfying the requirements of the ripple suppression function,

TABLE I
COMPARISON BETWEEN THE EXISTING AND THE PROPOSED APD METHODS

Aspects \ Methods	[21]	[28]	[30]	[33]	Buck- type method [32]	Proposed method
Compensator power/ nominal power	100%	100%	100%	15.0%	100%	11.6% (peak) 8.1% (average)
Soft-switching of APD part	No	Partial	No	No	No	Yes
Voltage boosting capability	No	Yes	No	Yes	No	Yes
Additional switches	Yes	No	No	Yes	No	No
Additional filter capacitor	Yes	No	Yes	Yes	No	No
APD effect for efficiency	Low	Moderate	Moderate	Moderate	Moderate	Low
Control and modulation complexity	Moderate	Moderate	Moderate	Low	Low	Low
Influence of deadtime on control	Yes	No	Yes	No	Yes	No

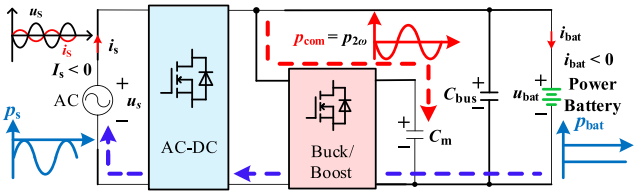

Fig. 12. EV charging system structure diagram in V2G mode when using the traditional buck type APD method.

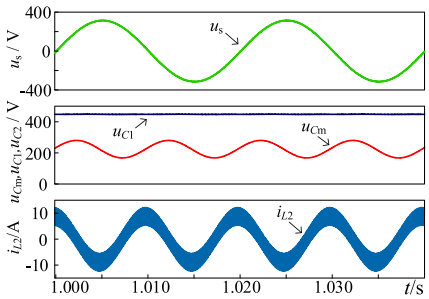

Fig. 13. Main simulation waveforms of the buck type APD method in the V2G mode.

the value of m is set as the maximum value, which reduces the voltage stress of the switches on the high-voltage side and widens the soft-switching range of the APD circuit.

C. Comparison Between the Existing APD Methods and the Proposed Method

A detailed comparison between the existing APD methods in recent literature and the proposed APD method is included, as shown in Table I. Among these methods, based on the structure of the auxiliary power charger, as shown in Fig. 12, the traditional buck-type APD method in [32] can be used to suppress the ripple power at twice the grid frequency in the charging system adopted in this article. By multiplexing the buck/boost and C_m and turning OFF the switches of the LLC converter, a buck-type APD circuit as shown in Fig. 2(a) can be formed. The comparison between the existing APD methods and the proposed APD method mainly contains the following eight aspects:

1) *Compensator power/nominal power:* In the existing methods, the power to be compensated by the APD circuit is generally equal to the ripple power $p_{2\omega}$ generated on the grid side, of which the amplitude is equal to the charging power $P_{\rm in}$ of the system, so these methods have higher requirements on the capacity of the APD part. Ignoring the power loss of the converter, in the proposed method, the relationship between the maximum value of the power $p_{\rm com}$ to be compensated by the APD circuit and the charging power $P_{\rm in}$ is as follows:

$$\frac{p_{\rm com\_max}}{P_{\rm in}} = \frac{u_{C2} i_{\rm bat}}{u_{\rm bat} i_{\rm bat}} = \frac{U_{\rm LVmax}}{u_{\rm bat}}. \tag{22}$$

It can be seen from (22) that with the proposed method, the compensator power of the APD circuit is significantly reduced, which can decrease the requirements on the capacity of the auxiliary power charger, and reduces the impact of power decoupling on the efficiency of the system.

2) *Soft-switching of APD part:* In the existing APD methods, it is relatively difficult to achieve wide-range soft-switching operation in the APD circuits. Taking the buck-type APD method in [32] as an example, since the compensator power by the APD circuit is relatively high, it is difficult to achieve zero-crossing of i_{L2} in each switching cycle, that is, it is hard to achieve soft-switching in the full load range. The corresponding simulation waveforms under full load is shown in Fig. 13. In contrast, it can be seen from the above analysis that the proposed APD method can achieve soft-switching of the switches in the buck/boost and the LLC converters.
3) *Voltage boosting capability:* According to (9), in the proposed method, the APD circuit is equivalent to a series-connected dc–Dc converter, and there is a $1/(1-m)$ boost ratio between the input and output voltages. This boost ratio can reduce the bus voltage of the system, and reduce the voltage stress and switching loss of the corresponding switches.
4) *Additional switches:* Since several methods multiplex the auxiliary power charger, it can be considered that no additional switches are required. However, the voltage and

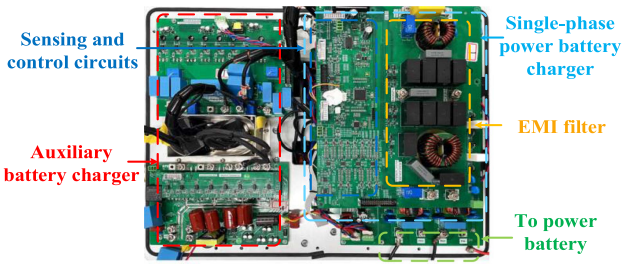

Fig. 14. Prototype of the single-phase EV onboard charger.

current stresses required by the existing APD methods are much higher than those of the proposed method, resulting in higher costs.

5) *Additional filter capacitor:* The bus capacitor $C_{\rm bus}$ in the proposed method can be decoupled from the output side and used together with C_2 in the APD circuit for power decoupling, which can further reduce the required capacitance in the charging system.
6) *APD effect for efficiency:* In the proposed method, the APD circuit requires less compensator power to process, and the switches of the APD circuit can operate under soft-switching. In addition, by selecting m, the lowest u_{C1} can be achieved while realizing the APD function, which can further improve the efficiency of the converter.
7) *Control and modulation complexity:* In the latter three control methods, the charging function and the APD function are decoupled, and thus the control schemes are easy to realize.
8) *Influence of deadtime on control performance:* In the modulation part, the deadtime will be added to the signals of the half-bridge switches, and the ripple suppression performance of the corresponding traditional methods will be affected. In contrast, the proposed method can make the waveform of i_{L2} have zero-crossing points within the full load range, and its control performance is not affected by the deadtime.

IV. Experimental Results and Analyses

In order to validate the feasibility and effectiveness of the proposed APD method, a 2-kW single-phase EV charger prototype is developed, as shown in Fig. 14. Its control methods are implemented in the microcontroller TMS320F28069 from Texas Instruments. The experimental parameters are listed in Table II.

Fig. 15 shows the waveforms of the input voltage and input current, dc voltage $u_{\rm bat}$, and current $i_{\rm bat}$ under half load in the V2G mode when the APD method is not adopted or the proposed APD method is adopted in the system, and the Fourier analysis diagram of the input current. When the converter is operating without the APD method, the distortion of the input current is larger, the total harmonic distortion (THD) of the input current is 2.43%, and the power factor is 0.9832. The ripple current of the power battery $\Delta i_{\rm bat}$ is 4.8 A, which is about twice of its dc component. With the APD method, it can be seen from Fig. 15(b) that the distortion of the input current is reduced, the THD$_i$ of the input current decreases to 1.92%, and the power factor is 0.9864. At the same time, the current ripple $\Delta i_{\rm bat}$ is suppressed to 0.8 A, reducing by 83.3%, and thus the APD function can be realized by adopting the proposed method. It is noted that with the proposed APD method, while the second-order current ripple is significantly reduced, the ripple components in the battery current above 100 Hz are increased. However, the ripple components in the mid- and high-frequency band accounts for a small proportion of the battery current, and their influence on the battery lifetime can be ignored compared to the second-order current ripple [37], [38]. In addition, it can be seen from the Fourier analysis diagram of the input current in Fig. 15(c) that with the proposed method, the THD$_i$ of the input current at half load is reduced by 0.51%, and the third, fifth, and seventh harmonic components are reduced by 72.2%, 38.7%, and 50.9%, respectively.

TABLE II
Experimental Parameters

Parameters	Values
AC voltage rms U_s/V	230
AC voltage frequency $f_{\rm grid}$/Hz	50
Power battery voltage $u_{\rm bat}$/V	450
Maximum voltage of C_2 $U_{\rm LVmax}$/V	52
Input filter inductor L_1/mH	1.2
Buck/Boost inductor L_2/mH	0.8
DC-bus capacitors $C_{\rm bus}$, C_2/μF	320, 30
Filter capacitor of Buck/boost $C_{\rm m}$/μF	10 (Proposed method), 250 (Traditional method)
PWM frequency of ac–dc converter $f_{\rm sab}$/kHz	20
PWM frequency of buck/boost $f_{\rm sm}$/kHz	20
PWM frequency of LLC $f_{\rm sLLC}$/kHz	68
Sampling frequency f_s/kHz	20
Rated output power $P_{\rm out}$/W	2000

Fig. 16 illustrates the dynamic waveform when the proposed APD method is adopted and the reference $u_{C2\rm ref}$ is gradually increased under full load in the V2G mode, and the steady-state waveform when the APD function is realized. When $U_{\rm apd}$ is set as zero, the ripple components of u_{C1} and u_{C2} are relatively small, while the ripple current $\Delta i_{\rm bat}$ of the power battery is 10.1 A. It can be seen that the ripple component of u_{C1} increases with the increase of the amplitude of $u_{C2\rm ref}$, thereby absorbing the ripple power at twice the grid frequency, while the ripple current $\Delta i_{\rm bat}$ of the battery gradually decreases to 1.4 A, reducing by 86.1%. In addition, the grid-side output power of the converter remains stable during the whole dynamic process. It is noted that with the proposed APD method, the impact of the second-order ripple power on the input current control performance is reduced, the grid-side power quality is improved, and the second-order ripple component in the battery current can be suppressed, which is conducive to extending the lifetime of the power battery.

To further verify the soft-switching operation of the APD circuit, the experimental results shown in Fig. 17 are obtained, when $P_{\rm out} = 2000$ W. It can be seen in Fig. 17(a) that in the proposed method, the bus capacitor $C_{\rm bus}$ and the dc output

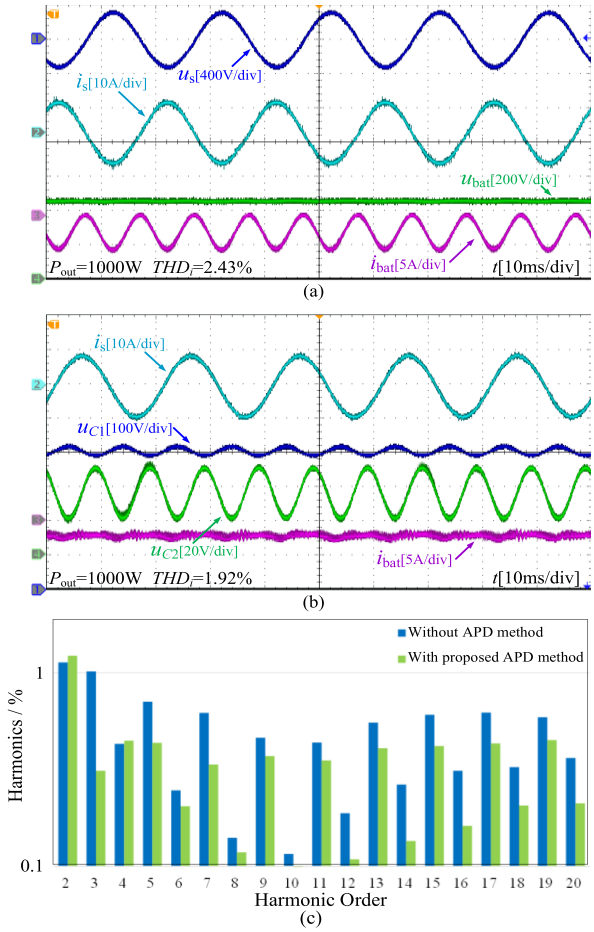

Fig. 15. Experimental waveforms of the input currents and dc output voltages and battery current: (a) without APD method, (b) with proposed APD method, and (c) Fourier analysis of the input currents when $P_{\rm out} = 1000$ W.

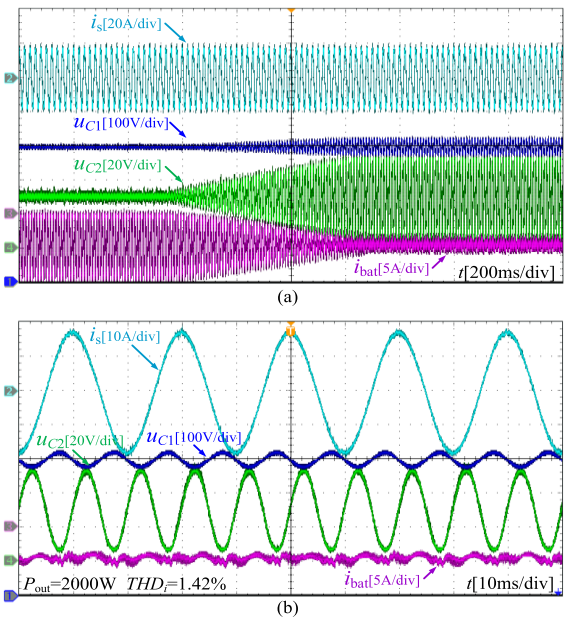

Fig. 16. Experimental waveforms of the input currents and DC output voltages and battery current with the proposed APD method when $P_{\rm out} = 2000$ W: (a) transient process and (b) steady state.

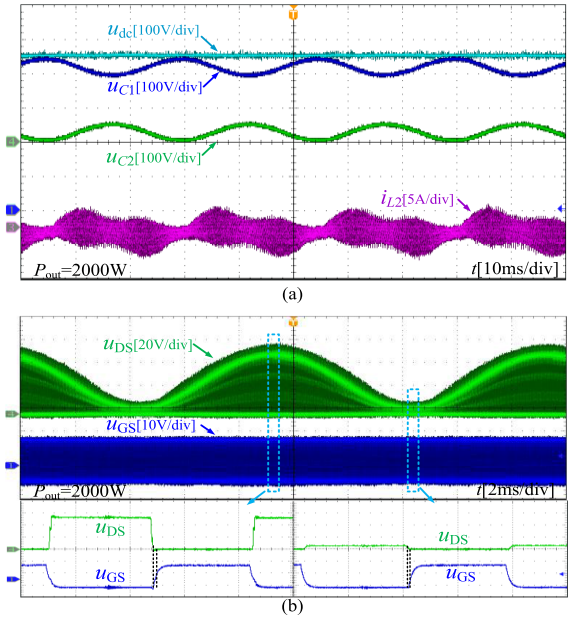

Fig. 17. Experimental waveforms of (a) input current, inductor current, and DC output voltages, and (b) ZVS in the low voltage side of LLC, converter with proposed APD method when $P_{\rm out} = 2000$ W.

TABLE III
SHARE OF THE RIPPLE POWER BY BUS CAPACITORS

Storage element	Power expression	Ripple power share
C_2, C_m in auxiliary battery charger	$-\frac{U_{\rm apd}}{u_{\rm bat}} p_{2\omega}$	3.45% (half load) 6.12% (rated load)
$C_{\rm bus}$ in power battery charger	$(1+\frac{U_{\rm apd}}{u_{\rm bat}}) p_{2\omega}$	103.45% (half load) 106.12% (rated load)

voltage are decoupled, and the second-order ripple power is suppressed through the voltage fluctuation of u_{C1} and u_{C2}, while the low-frequency ripple components of $u_{\rm bat}$ is very small. The voltage stress of the high-voltage side switches is therefore lower than $u_{\rm bat}$.

In addition, it is noted that the peak value of the compensator power that the APD circuit needs to compensate in the proposed method is $U_{\rm LVmax}/u_{\rm bat}$, which is about 11.56% of the rated power, while the average power in the APD circuit is $mP_{\rm in}$, which is 8.11% of the rated power at half load, and 5.44% of the rated power at full load. The share of the ripple power of the capacitors can be calculated from (8) and (22), as listed in Table III. It can be seen that the proposed APD method increases the ripple power that $C_{\rm bus}$ needs to absorb, while the APD circuit only needs to compensate less than 10% of the ripple power to indirectly control the voltage variation of $C_{\rm bus}$. Therefore, the converter realizes that the waveform of i_{L2} has zero-crossing points in every switching cycle, thus realizing the ZVS turn-ON of the buck/boost switches. Moreover, the key waveforms of the LLC are shown in Fig. 17(b), where $u_{\rm GS}$ and $u_{\rm DS}$ are the gate–source voltage and the drain–source voltage of S_{11} at the low-voltage side of the LLC converter, respectively. It can be

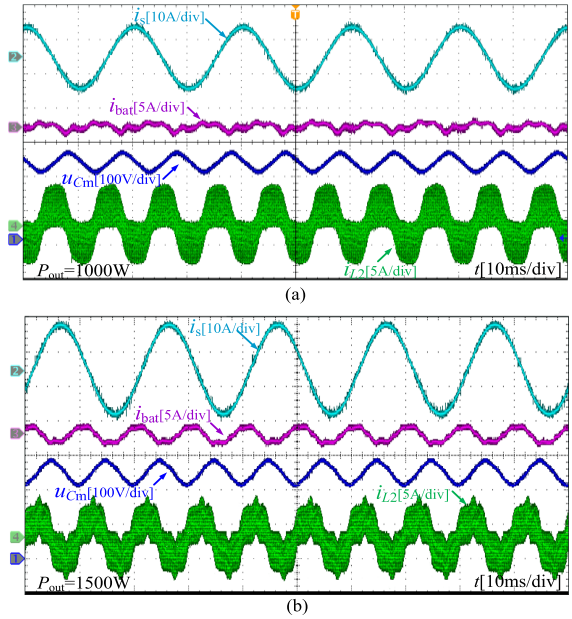

Fig. 18. Experimental waveforms of the input current, inductor current, DC output voltage, and battery current with the traditional buck type APD method (a) when $P_{\rm out}$ = 1000 W and (b) when $P_{\rm out}$ = 1500 W.

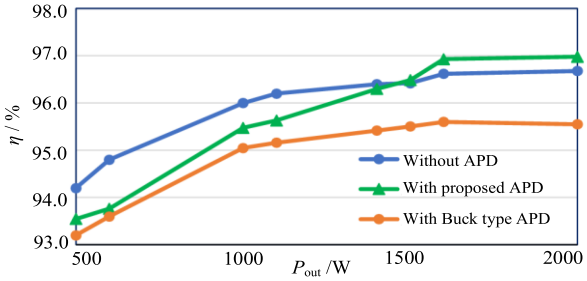

Fig. 19. Efficiency of the converter with different methods.

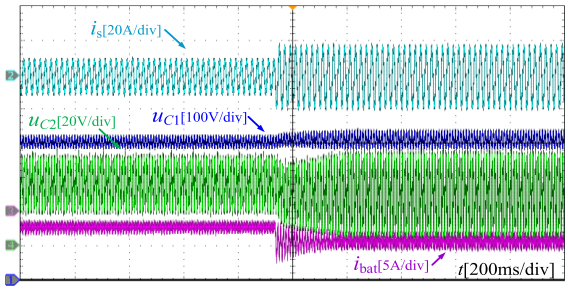

Fig. 20. Experimental waveforms of the input currents and DC output voltages and battery current with the proposed APD method when $P_{\rm out}$ steps from 1000 to 2000 W.

seen from Fig. 17(b) that ZVS turn-ON can also be realized by the switches at the low-voltage side of the LLC converter during the V2G operation, which can reduce the switching loss when using the proposed APD scheme.

In order to further validate the performance of the proposed method, a comparative experiment with the buck-type APD method is carried out by increasing the capacitance of C_m to 250 μF and turning OFF the switches of the LLC, and the experimental waveforms are shown in Fig. 18. It can be seen from Fig. 18(a) that under the half load, by controlling the waveform of u_{Cm}, the ripple power can be suppressed and the ripple $\Delta i_{\rm bat}$ of the power battery current is reduced to 1.6 A. The converter can achieve the zero-crossing of i_{L2} in each switching cycle, that is, the buck/boost can realize ZVS operation. However, due to the nonlinear effect of deadtime, the waveform of i_{L2} is distorted, which affects the voltage control performance of u_{Cm}, resulting in a higher low-frequency ripple of the battery current with the buck-type APD method. As shown in Fig. 18(b), with the buck-type APD method, the second-order ripple power generated on the grid side needs to be fully compensated by buck/boost converter, and thus i_{L2} is relatively large when $P_{\rm out}$ = 1500 W. However, as the control performance is affected by the deadtime, it is difficult for the converter to suppress the low-frequency ripple current of the battery and $\Delta i_{\rm bat}$ is about 2.2 A.

The efficiency curves of the charging system without APD methods and with the proposed method and the buck-type APD method are shown in Fig. 19. It can be seen that the efficiency of the converter with the traditional buck APD method is the lowest, which is reduced by about 1% compared with that without APD methods. The efficiency with the proposed method is slightly higher than that with the buck APD method before the half load, but lower than that without APD methods. However, when the output power is more than 3/4 times the rated power, the proposed APD method has the highest operating efficiency of 96.95%, which is 0.3% higher than that without APD schemes. It is noted that since the proposed method reduces the voltage stress of the switches on the high-voltage side of the converter and the APD circuit only needs to compensate less than 1/10 of the rated power with achieving soft-switching operation, it has higher efficiency than that with the traditional method.

To verify the dynamic performance of the proposed method, Fig. 20 shows the experimental results when the output power of the converter steps from 1 to 2 kW. It can be seen from Fig. 20 that after the output power of the converter is increased, in order to make the instantaneous value of u_{C2} not exceed $U_{\rm LVmax}$, the control scheme first calculates the required m according to the output power, reduces the average voltage of u_{C2}, and then gradually increases the amplitude $U_{\rm apd}$ of the reference voltage to realize the APD function in the steady state. It can be seen from the experiments that the proposed method can realize the second-order ripple current suppression of the battery under different powers, and thus prolong the lifetime of the power battery. In addition, the proposed method can make the average value of u_{C2} the highest while ensuring that there is no overvoltage at the low-voltage side, thereby reducing the voltage stress of the high-voltage side switches and improving the efficiency of the converter.

V. Conclusion

This article presents an integrated APD method suitable for the V2G application in the single-phase EV charging system.

In the proposed method, a series-connected dc–dc converter is formed by multiplexing the auxiliary power charger and the bus capacitors are all used for the second-order ripple current suppression of the battery, which reduces the required bus capacitance of the converter, improves the power quality of the grid side, and contributes to the extension of the power battery lifetime. Compared to the existing APD methods, the proposed method does not require additional switches or energy storage devices. In addition, the compensator power of the APD circuit is less than 10% of the rated power, while the soft-switching operation is achieved in the proposed APD circuit. Furthermore, with the corresponding control method, the voltage stress of the high-voltage side switches can be advantageously reduced, which further improves the efficiency of the converter. Finally, experimental results verify that the proposed method has better steady-state performance than the traditional method, making it suitable for application in the single-phase EV charging system. It is found that although the power efficiency achieved by the proposed method is slightly lower than that without APD methods before the half load, however, the proposed APD method achieves the highest operating efficiency of 96.95% at heavy load, which is 0.3% higher than that without APD schemes.

REFERENCES

[1] A. Khaligh and S. Dusmez, "Comprehensive topological analysis of conductive and inductive charging solutions for plug-in electric vehicles," *IEEE Trans. Veh. Technol.*, vol. 61, no. 8, pp. 3475–3489, Oct. 2012.

[2] G. Buja, M. Bertoluzzo, and C. Fontana, "Reactive power compensation capabilities of V2G-enabled electric vehicles," *IEEE Trans. Power Electron.*, vol. 32, no. 12, pp. 9447–9459, Dec. 2017.

[3] Y. Zhang, S. Gao, S. Jing, and X. Huang, "Soft-switching operation with a variable switching frequency control for switched-quasi-Z-source bidirectional DC–DC converter in EVs," *IEEE Trans. Ind. Electron.*, vol. 70, no. 1, pp. 384–395, Jan. 2023.

[4] U. Sharma and B. Singh, "A bidirectional onboard charger with multistep constant current charging capability," *IEEE Trans. Transp. Electrific.*, vol. 9, no. 1, pp. 1227–1237, Mar. 2023.

[5] M. C. Kisacikoglu, M. Kesler, and L. M. Tolbert, "Single-phase on-board bidirectional PEV charger for V2G reactive power operation," *IEEE Trans. Smart Grid*, vol. 6, no. 2, pp. 767–775, Mar. 2015.

[6] L. Peng, L. Ma, W. Song, and H. Liu, "A simple model predictive instantaneous current control for single-phase PWM converters in stationary reference frame," *IEEE Trans. Power Electron.*, vol. 37, no. 7, pp. 7629–7639, Jul. 2022.

[7] P. Wang, Y. Bi, F. Gao, T. Song, and Y. Zhang, "An improved deadbeat control method for single-phase PWM rectifiers in charging system for EVs," *IEEE Trans. Veh. Technol.*, vol. 68, no. 10, pp. 9672–9681, Oct. 2019.

[8] Y. Ohnuma, K. Orikawa, and J.-I. Itoh, "A single-phase current-source PV inverter with power decoupling capability using an active buffer," *IEEE Trans. Ind. Appl.*, vol. 51, no. 1, pp. 531–538, Jan./Feb. 2015.

[9] S. S. Zhang, "The effect of the charging protocol on the cycle life of a li-ion battery," *J. Power Sources*, vol. 161, no. 2, pp. 1385–1391, Oct. 2006.

[10] H. Wang, H. Wang, G. Zhu, and F. Blaabjerg, "An overview of capacitive DC-links-topology derivation and scalability analysis," *IEEE Trans. Power Electron.*, vol. 35, no. 2, pp. 1805–1829, Feb. 2020.

[11] D. Neumayr, D. Bortis, and J. W. Kolar, "The essence of the little box challenge-Part A: Key design challenges solutions," *CPSS Trans. Power Electron. Appl.*, vol. 5, no. 2, pp. 158–179, 2020.

[12] D. Neumayr, G. C. Knabben, E. Varescon, D. Bortis, and J. W. Kolar, "Comparative evaluation of a full- and partial-power processing active power buffer for ultracompact single-phase DC/AC converter systems," *IEEE J. Emerg. Sel. Topics Power Electron.*, vol. 9, no. 2, pp. 1994–2013, Apr. 2021.

[13] Y. Zhang, J. Fang, F. Gao, T. Song, S. Gao, and D. J. Rogers, "Second-harmonic ripple voltage suppression of integrated single-phase pulsewidth modulation rectifier charging system for EVs," *IEEE Trans. Power Electron.*, vol. 35, no. 4, pp. 3616–3626, Apr. 2020.

[14] Y. Sun, Y. Liu, M. Su, W. Xiong, and J. Yang, "Review of active power decoupling topologies in single-phase systems," *IEEE Trans. Power Electron.*, vol. 31, no. 7, pp. 4778–4794, Jul. 2016.

[15] L. Shen, J. Chen, Z. Jin, Z. Liu, D. Zhou, and C. Wu, "Resonating power decoupling using multifunctional bidirectional DC/DC converter in hybrid railway traction application," *IEEE Trans. Power Electron.*, vol. 37, no. 1, pp. 404–415, Jan. 2022.

[16] X. Huang, X. Ruan, J. Fang, and S. Kan, "A virtual impedance based control scheme for modular electrolytic capacitor-less second harmonic current compensator," *IEEE Trans. Ind. Electron.*, vol. 68, no. 1, pp. 198–209, Jan. 2021.

[17] X. Cao, Q.-C. Zhong, and W.-L. Ming, "Ripple eliminator to smooth DC-bus voltage and reduce the total capacitance required," *IEEE Trans. Ind. Electron.*, vol. 62, no. 4, pp. 2224–2235, Apr. 2015.

[18] H. Zhang, X. Li, B. Ge, and R. S. Balog, "Capacitance, DC voltage utilization, and current stress: Comparison of double-line frequency ripple power decoupling for single-phase systems," *IEEE Ind. Electron. Mag.*, vol. 11, no. 3, pp. 37–49, Sep. 2017.

[19] W. Qi, H. Wang, X. Tan, G. Wang, and K. D. T. Ngo, "A novel active power decoupling single-phase PWM rectifier topology," in *Proc. IEEE Appl. Power Electron. Conf. Expo.*, 2014, pp. 89–95.

[20] J. Xu, T. B. Soeiro, F. Gao, H. Tang, and P. Bauer, "Minimum switching losses discontinuous PWM strategy for bidirectional single-phase AC–DC converter with active power decoupling circuit," *IEEE Trans. Power Electron.*, vol. 36, no. 5, pp. 6118–6132, May 2021.

[21] J. Xu, T. B. Soeiro, F. Gao, H. Tang, and P. Bauer, "Carrier-based generalized discontinuous PWM strategy for single-phase three-legs active power decoupling converters," *IEEE Trans. Ind. Electron.*, vol. 68, no. 11, pp. 11609–11613, Nov. 2021.

[22] Y. Tang and F. Blaabjerg, "A component-minimized single-phase active power decoupling circuit with reduced current stress to semiconductor switches," *IEEE Trans. Power Electron.*, vol. 30, no. 6, pp. 2905–2910, Jun. 2015.

[23] J. Zhang, L. He, and Z. Lin, "Fractional-order-based low-order harmonic current suppression method considering asymmetrical capacitor parameters," *IEEE Trans. Power Electron.*, vol. 38, no. 3, pp. 3775–3784, Mar. 2023.

[24] H. V. Nguyen, D.-D. To, and D.-C. Lee, "Onboard battery chargers for plug-in electric vehicles with dual functional circuit for low-voltage battery charging and active power decoupling," *IEEE Access*, vol. 6, pp. 70212–70222, 2018.

[25] Y. Tang, Z. Qin, F. Blaabjerg, and P. C. Loh, "A dual voltage control strategy for single-phase PWM converters with power decoupling function," *IEEE Trans. Power Electron.*, vol. 30, no. 12, pp. 7060–7071, Dec. 2015.

[26] Y. Wang and R.-J. Wai, "Adaptive power decoupling strategy for single-phase grid-connected converter," *IEEE Trans. Ind. Appl.*, vol. 55, no. 4, pp. 4275–4285, Jul./Aug. 2019.

[27] S. Xie et al., "Adaptive power decoupling control for single-phase converter with unbalanced DC-split-capacitor circuit," *IEEE Trans. Power Electron.*, vol. 36, no. 10, pp. 12127–12136, Oct. 2021.

[28] Z. Li et al., "A second-harmonic suppression method based on differentiated-capacitance design for input-parallel output-series DAB fed single-phase VSI," *IEEE Trans. Power Electron.*, vol. 37, no. 10, pp. 11592–11606, Oct. 2022.

[29] R. Hou and A. Emadi, "Applied integrated active filter auxiliary power module for electrified vehicles with single-phase onboard chargers," *IEEE Trans. Power Electron.*, vol. 32, no. 3, pp. 1860–1871, Mar. 2017.

[30] H. V. Nguyen, D.-C. Lee, and F. Blaabjerg, "A novel SiC-based multifunctional onboard battery charger for plug-in electric vehicles," *IEEE Trans. Power Electron.*, vol. 36, no. 5, pp. 5635–5646, May 2021.

[31] R. Hou and A. Emadi, "A primary full-integrated active filter auxiliary power module in electrified vehicles with single-phase onboard chargers," *IEEE Trans. Power Electron.*, vol. 32, no. 11, pp. 8393–8405, Nov. 2017.

[32] Y. Zhang, J. Fang, F. Gao, S. Gao, D. J. Rogers, and X. Zhu, "Integrated high- and low-frequency current ripple suppressions in a single-phase onboard charger for EVs," *IEEE Trans. Power Electron.*, vol. 36, no. 2, pp. 1717–1729, Feb. 2021.

[33] E. Heydari, A. Y. Varjani, and D. Diallo, "A dual-function power decoupling circuit for single-stage grid-connected PV inverter," *IEEE Trans. Power Electron.*, vol. 37, no. 6, pp. 7422–7431, Jun. 2022.

[34] H. Li, M. Liu, Y. Yang, Z. Song, and Y. Wang, "A multi-MHz active clamp topology for high cost-performance wireless power transfer," *IEEE Trans. Power Electron.*, vol. 37, no. 10, pp. 12828–12840, Oct. 2022.

[35] J. Xu, T. B. Soeiro, Y. Wang, F. Gao, H. Tang, and P. Bauer, "A hybrid modulation featuring two-phase clamped discontinuous PWM and zero voltage switching for 99% efficient DC-type EV charger," *IEEE Trans. Veh. Technol.*, vol. 71, no. 2, pp. 1454–1465, Feb. 2022.
[36] Y. Bi et al., "Modified deadbeat predictive current control method for single-phase AC–DC PFC converter in EV charging system," *IEEE Trans. Ind. Electron.*, vol. 70, no. 1, pp. 286–297, Jan. 2023.
[37] M. Uno and K. Tanaka, "Influence of high-frequency charge–discharge cycling induced by cell voltage equalizers on the life performance of lithium-ion cells," *IEEE Trans. Veh. Technol.*, vol. 60, no. 4, pp. 1505–1515, May 2011.
[38] W. Vermeer, M. Stecca, G. R. C. Mouli, and P. Bauer, "A critical review on the effects of pulse charging of li-ion batteries," in *Proc. IEEE 19th Int. Power Electron. Motion Control Conf.*, 2021, pp. 217–224.

Yuxuan Bi was born in Hebei, China. He received the B.S. degree in electrical engineering from the Dalian University of Technology, Dalian, China, in 2017, and the M.S. degree in electrical engineering from the Tianjin University, Tianjin, China, in 2020. He is currently working toward the Ph.D. degree in electrical engineering with the Shanghai Jiao Tong University, Shanghai, China.

His research interests include ac–dc converters and energy management of electric vehicles.

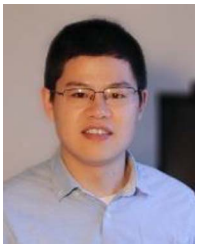

Chao Wu (Member, IEEE) was born in Hubei Province, China. He received the B.Eng. degree from the Hefei University of Technology, Hefei, China, in 2014, and the Ph.D. degree from the Zhejiang University, Hangzhou, China, in 2019, both in electrical engineering.

From 2019 to 2021, he was a Postdoctoral Researcher with the Department of Energy Technology, Aalborg University, Aalborg, Denmark. He is currently an Assistant Professor with the Department of Electrical Engineering, Shanghai Jiao Tong University, Shanghai, China. He has authored/coauthored more than 20 IEEE/IET Transaction papers. His research interests include modeling, control, and stability analysis of power electronics in renewable energy applications, particularly the control and operation of doubly fed induction generators for dc connection and the transient stability of power converters.

Junzhong Xu (Member, IEEE) was born in Ningbo, China, in 1994. He received the B.S. degree in electrical engineering from the Harbin Institute of Technology, Harbin, China, in 2016, and the Ph.D. degree in electrical engineering from the Shanghai Jiao Tong University, Shanghai, China, in 2021.

From 2020 to 2021, he was a Visiting Scholar with the DC Systems, Energy Conversion and Storage Group, Delft University of Technology, Delft, The Netherlands. He worked as a Postdoctoral Research Fellow with the Department of Electrical Engineering, Shanghai Jiao Tong University, Shanghai, China, in 2021. He is currently working with the Power Electronic Systems Laboratory, the Swiss Federal Institute of Technology, Zurich, Switzerland. His research interests include advanced control and modulation for power converters.

Dr. Xu was the recipient of the Outstanding Ph.D. Thesis Award from the Shanghai Jiao Tong University in 2021.

Houji Li (Student Member, IEEE) was born in Tai'an, China, in 1996. He received the B.S. and M.S. degrees in electrical engineering from the Qingdao University, Qingdao, China, in 2017 and 2020, respectively. He is currently working toward the Ph.D. degree in electrical engineering with the Shanghai Jiao Tong University, Shanghai, China.

His research interests include wireless power transfer and battery management systems.

Mr. Li was the recipient of the Best Student Paper Prize of IEEE WoW in 2021.

Yong Wang (Member, IEEE) received the Ph.D. degree in power electronics from the Zhejiang University, Hangzhou, China, in 2005.

From 2005 to 2008, he was a Senior Researcher with the Samsung Advanced Institute of Technology, Suwon, South Korea, working on the fuel cell grid tied inverter. From 2008 to 2010, he was working with the Danfoss Solar Inverters, Soenderborg, Denmark, as a power electronics Hardware Engineer. In the year 2010, he joined the Shanghai Jiao Tong University, Shanghai, China, where he is currently a Full Professor with the Department of Electrical Engineering. His research interests include new energy storage system and electric vehicle power supply system.

Guohua Shu was born in Zhejiang, China, in 1969. He received the M.S. degree in electrical engineering from the Shanghai Jiao Tong University, Shanghai, China, in 1996.

Since 1996, he has been a Teacher and a Researcher with the Shanghai Jiao Tong University, where he is currently a Professor and the Director of the Electrical and Electronic Experiment Center. His research interests include power electronics, computer control technology, and embedded system application.

Thiago Batista Soeiro (Senior Member, IEEE) received the B.S. (Hons.) and M.S. degrees in electrical engineering from the Federal University of Santa Catarina, Florianopolis, Brazil, in 2004 and 2007, respectively, and the Ph.D. degree from the Swiss Federal Institute of Technology, Zurich, Switzerland, in 2012.

During the Master and Ph.D. studies, he was a Visiting Scholar with the Power Electronics and Energy Research Group, Concordia University, Montreal, QC, Canada, and with the Center for Power Electronics Systems, Blacksburg, VA, USA, respectively. From 2012 to 2013, he was a Researcher with the Power Electronics Institute, Federal University of Santa Catarina. From October 2013 to April 2018, he was with the Corporate Research Center, ABB Switzerland Ltd., Baden-Dattwil, Switzerland, where he was a Senior Scientist. From May 2018 to January 2022, he was with the DC Systems, Energy Conversion and Storage Group, Delft University of Technology, Delft, The Netherlands, where he was an Associate Professor. From January to October 2022, he was with the Power Management and Distribution Section for the European Space Research and Technology Centre, Noordwijk, The Netherlands. Since October 2022, he has been a Full Professor for Power Electronics with the Power Electronics and EMC Group, University of Twente, Enschede, The Netherlands. His research interests include advanced high-power converters and dc system integration.

Dr. Soeiro was a recipient of the 2013 IEEE Industrial Electronics Society Best Conference Paper Award and the Best Paper Awards in the following IEEE conferences: International Conference on Power Electronics (ECCE Asia 2011), the International Conference on Industrial Technology (ICIT 2013), the Conference on Power Electronics and Applications EPE'15 (ECCE Europe 2015), and the International Conference on Power Electronics and Motion Control 2020 and 2022 (PEMC 2020 and 2022).